Current Biology, Volume *27*

Supplemental Information

The Function and Organization of the Motor System Controlling Flight Maneuvers in Flies

Theodore Lindsay, Anne Sustar, and Michael Dickinson

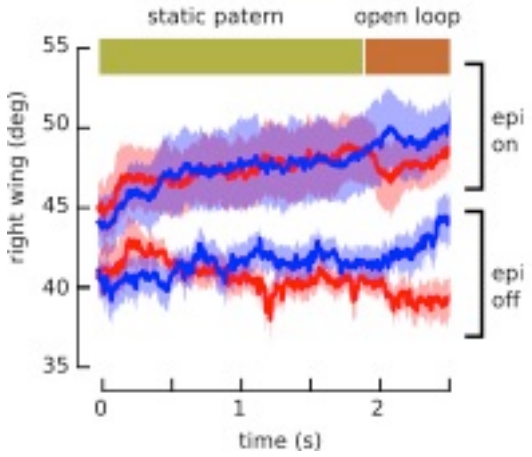

Figure S1. Related to Figure 1. Effect of blue epi-illumination on stroke amplitude. The amplitude of the ipsilateral (right) wing stroke amplitude during a two second presentation of a static visual stimulus followed by a 500 ms presentation of open-loop rightward (red) and leftward (blue) motion around the yaw axis. Prior to time zero the flies were engaged in closed-loop stripe fixation. A slow elevation in wing-stroke amplitude was evident in trials where the blue epi-illumination light used to image GCaMP6f was turned on (epi-on) and absent in trials where this light was off.

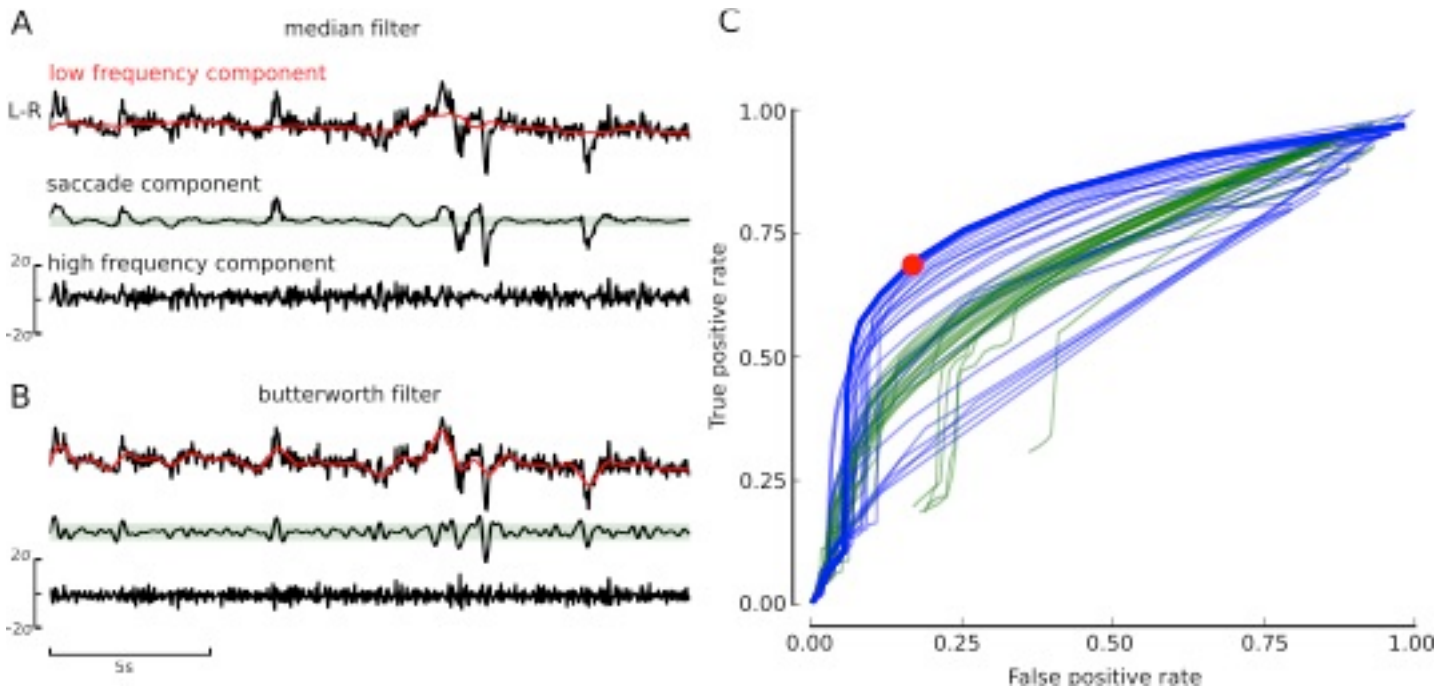

Figure S2. Related to Figure 3. Methods and evaluation of parameters used to detect saccades. Tethered flight saccades are qualitatively distinct behavioral motifs characterized by a short duration spike in yaw torque -- a signal that is proportional to the left-right stroke amplitude (L-R). Our approach for detecting saccades centered on filtering the L-R signal to distinguish large transient spikes from both slow fluctuations and small high frequency changes that we interpret as measurement noise. We then classified saccades as epochs of the filtered L-R signal that crossed a set threshold. Although saccades are subjectively easy to identify by visual inspection of the L-R records, inspection of the signal statistics did not expose any natural clusters or discontinuities that would inform filter settings or threshold levels. Therefore, we evaluated the parameters of our classification routine against 486 manually annotated saccades taken from 94 trials. We considered two filtering approaches. (A) The low frequency (top trace, red) and high frequency (bottom, black) components that were rejected from an example sequence using a 1-3.5 Hz bandpass Butterworth filter. Saccades were identified by transients that deviated above or below a threshold of +/- 0.31σ. (B) As in A, the same sequence was subjected to a median filter with a kernel width of 81 samples (1.7s) to extract the slow components (top trace, red) and was followed by a weighted boxcar filter with a kernel width of 31 samples (0.65s) to reject high frequency noise (bottom trace, black). Saccades were identified as extrema above and below a threshold of +/- 0.15σ. We evaluated both approaches over a range of settings and threshold values by applying our automatic classifier to the manually annotated data set and calculating the true positive rate as TP/(TP+FN) and the false positive rate as FP/(FP+TN), where TP is the number of samples both manually and automatically classified as a saccade, TN is the number of samples both manually and automatically rejected as belonging to a saccade, FP is the number of samples automatically but not manually classified as a saccade, and FN is the number of samples manually classified as a saccade but automatically rejected. (C) The receiver operator characteristics for all the filtering settings as the threshold levels were varied. Classifiers built using the median/boxcar filters are shown in blue, those constructed using the Butterworth filter are shown in green. We chose to use a median/boxcar approach with the filter settings indicated in panel A that yielded a true positive rate of 0.69 and a false positive rate of 0.17 (red dot in C).

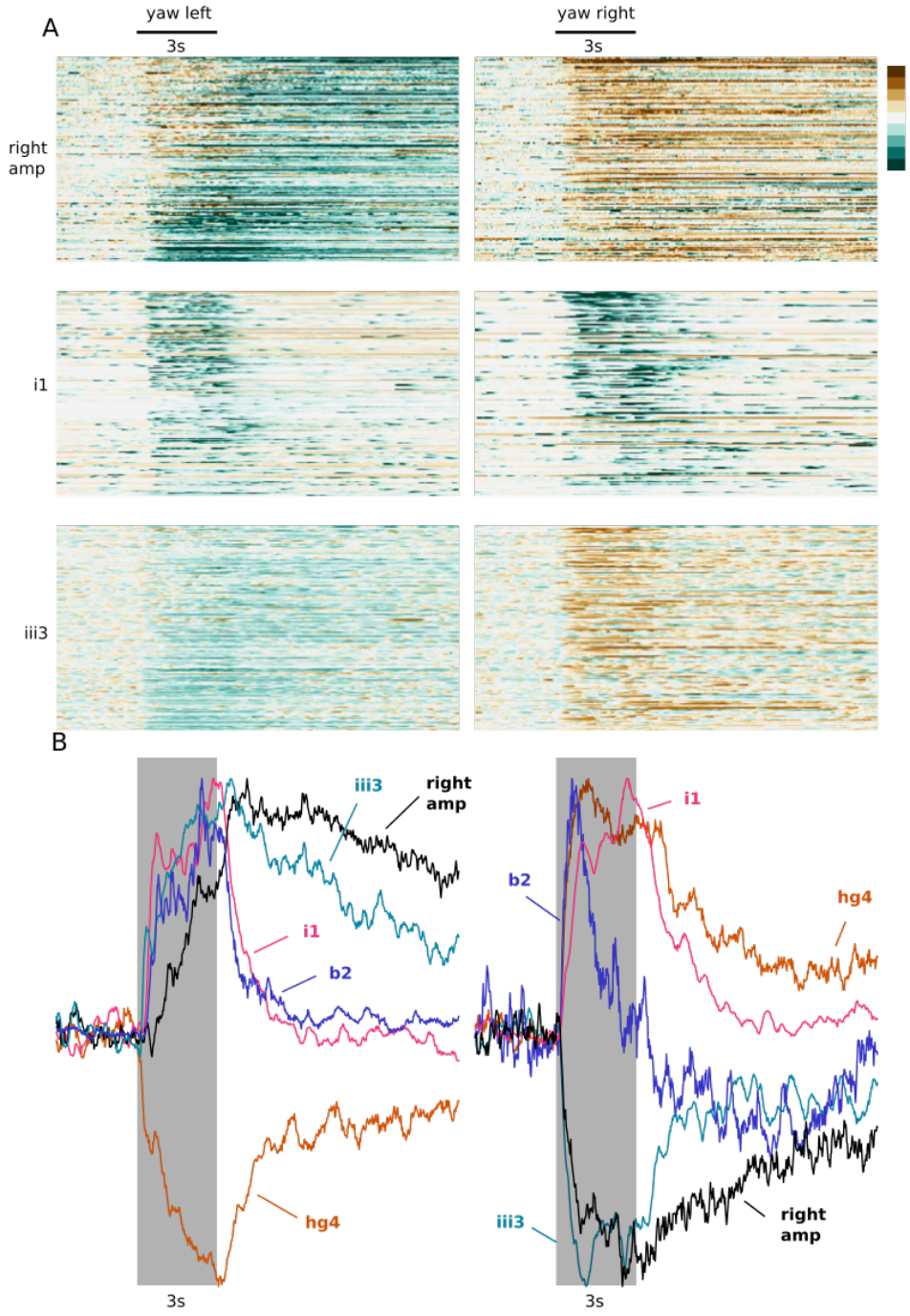

Figure S3. Related to Figure 5. Dynamics of muscle calcium and wing kinematics during visual motion around the yaw axis. (A) Raster plots of a subsample (200 out of 1150 total trails) that show the ipsilateral stroke amplitude (right amp) and the corresponding calcium signals of the i1 and iii3 muscles in response to a 3 second episode of yaw motion to the left or right (black bars, top). The rows of the rasters are sorted in descending order according to the average magnitude of ipsilateral stroke amplitude during the six seconds following stimulus onset. Note that for most trials (including both leftward and rightward motion) the phasic muscle i1 exhibited an increase in the rate of transient episodes of activation - a phenomenon that is primarily restricted to the stimulus motion epoch. In contrast, the tonic muscle iii3 responded to rightward motion with a rapid increase in activity that remained elevated long after the stimulus ended. During leftward motion, iii3 exhibited a decrease in activity that that outlasted the stimulus. (B) Ensemble averages of stroke amplitude overlaid by average calcium signals from four steering muscles. The signals were scaled to facilitate comparison of the response dynamics. The phasic muscles i1 and b2 responded with a transient increase in activity during both leftward and rightward right visual motion. In contrast, the average iii3 signal more closely followed both the dynamics and polarity of stroke amplitude. The tonic muscle hg4 displayed a behavior similar to iii3 but with reversed polarity. Color scale runs (from brown to green), -20° to 20° for stroke amplitude and -4σ to 4σ for calcium signals.

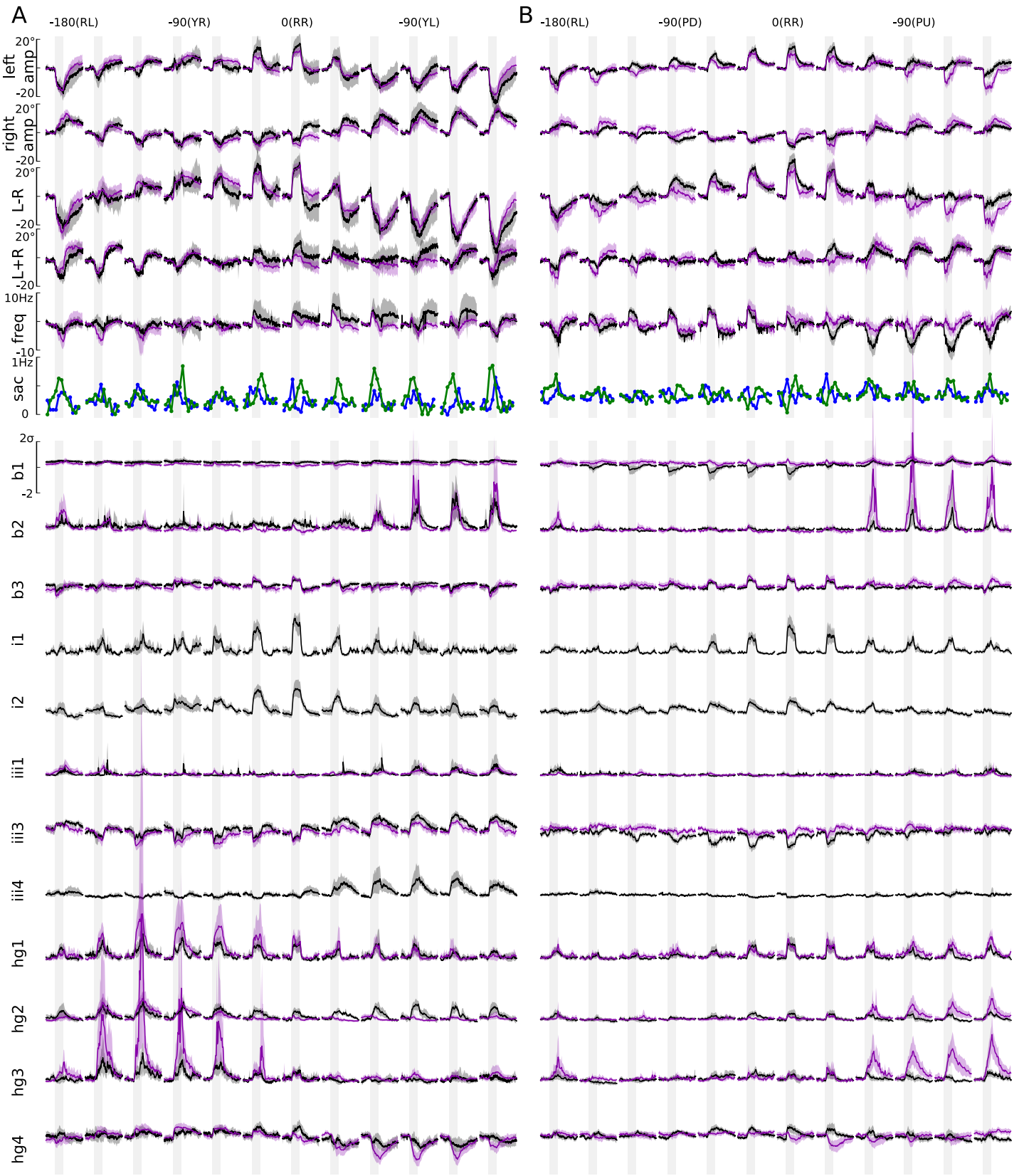

Figure S4. Related to Figure 7. Ensemble time-course of all kinematic and calcium signals collected in response to rotatory stimuli in midsagittal and azimuthal planes. (A) Rotational axes in the midsagittal plane. (B) Rotational axes in the azimuthal plane. Coordinates of stimulus are as in Figure 6. In addition to the ipsilateral wing stroke amplitude (right amp) data from the contralateral wing (left amp), the left + right (L+R) and left-right (L-R) stroke amplitude and wingstroke frequency (freq) are shown. Data used to construct peri-stimulus time histograms of leftward (blue) and rightward (green) saccade frequency (sac) were pooled from both genotypes used in the study. For all other signals results from GMR22H05 are shown in black, GMR39E01 in magenta.

Envelopes are 95% confidence intervals.

Supplemental Experimental Procedures

Visual stimuli

We presented motion stimuli using a cylindrical panoramic visual display constructed from LED panels as previously described but using 470nm peak wavelength. We lined the inside of the arena with a blue filter (Rosco no. 59 indigo) to ensure that light from the stimulus display did not contaminate the image stream. The display was constructed to extend azimuthally around the entire visual axis and filled 55° in elevation; however, the placement of the objective obscured a 3.2 sr solid angle or ~50% of a spherical visual field on the side ipsilateral to the muscles being imaged. We constructed patterns of visual motion by rotating and translating a virtual cloud of random point sources at a density of 8 points per cubic meter that we projected onto the cylindrical coordinates of the display. The intensity of each point source was attenuated according to the inverse square of the distance, and the projection was rendered onto the 92 by 36 pixel arena display at 3-bit grayscale resolution by down-sampling each frame through a 4-level Gaussian image pyramid. We simulated rotational motion at 90° s^{-1} and translational motion at 0.3 m s^{-1}. During rotational stimuli these patterns generated a broad-band spectrum of temporal frequencies along the rotational equator with a corner frequency of 2.5 Hz and a roll-off of 2 dB $decade^{-1}$. We designed three stimulus sets that we presented to three cohorts of animals. The first cohort provided the data presented in Figures 1-5 and consisted of rotational motion around the yaw axis and vertical translational motion. In other cohorts we examined rotational motion around the axes set in the vertical (cohort 2) and sagittal plane (cohort 3) that provided the data presented in Figure 7. In all cases, the order of the open loop stimuli was randomized and each motion trial was flanked by of an epoch in which we presented the static pattern (10 seconds for cohort 1, and 7 seconds for cohorts 2 and 3). In all cohorts, each trial was interleaved by a 5 second epoch of closed-loop stripe fixation.

Image un-mixing

Our method for un-mixing calcium signals is similar to previous blind approaches for extracting signals from intermingled sources; however, we took advantage of the highly stereotyped anatomy of *Drosophila* to construct a prior model of the spatial distribution of sources in the image stream. To construct a prior model of muscle morphology, we collected a z-stack of a phalloidin-stained hemithorax directly through the cleared cuticle with a voxel pitch of $(p_x, p_y, p_z) = (0.76, 0.76, 2.98)\ \mu$m in the x, y, z dimensions, where x, y and z are aligned with the anterior-posterior, dorsal-ventral and medial-lateral anatomical axes, respectively. A bright-field reference stack was simultaneously collected and used to identify correspondence points between the confocal stack and the calcium imaging sequence.

To extract the activation signals emanating from the array of j steering muscles we assumed that the observed time series of k fluorescent images with m pixels each, was generated from a non-negative linear combination of prior spatial distributions of the muscles, and the time series of their respective activations such that (following the notation used in regression):

$$\mathbf{XB} = \mathbf{Y},$$

where $\mathbf{Y}$ consists of k columns of vectorized images collected by the camera, $\mathbf{B}$ consists of k columns of unknown, positive j-dimensional column vectors of muscle activation, $\mathbf{X}$ is a design matrix that consists of j columns, each containing a vectorized model of the expected image of each muscle as viewed by the camera. We generated the model, $\mathbf{x_i}$ for each muscle i, $\mathbf{X} = [\mathbf{x_1} \cdots \mathbf{x_j}]$ from binary images that we manually segmented from 150 confocal optical sections of a phalloidin-stained hemithorax. We accounted for the depth of field of the objective lens by convolving each segmented confocal section, $\mathbf{S_{i,z}}$, with a circular kernel $\mathbf{C}(z)$ with a diameter d that depended on the depth, z, and then normalized the image of the convolved section so that the sum of the blurred pixel intensities matched the number of segmented pixels within $\mathbf{S_{i,z}}$. Thus, with $*$ indicating image convolution, we generated $\mathbf{x_i}$ by summing together the blurred, normalized, slices so that:

$$\mathbf{G}^*(i,z) = \mathbf{C}(z) * \mathbf{S_{i,z}}$$
$$\mathbf{x_i} = vec\left(\sum_{z=1}^{230} \mathbf{G}^*(i,z)\frac{\sum \mathbf{G}^*(z,i)}{\sum \mathbf{S_{i,z}}}\right).$$

The diameter of the blur circle $d(z)$, was calculated from a thin lens model specified by the microscope objective, and was a function depth of the section above and below the assumed focal plane so that:

$$d(z) = 2 \cdot f \cdot NA\frac{|p_z(z_i - l_o)|}{p_z z_i} + w,$$

where f and NA are the focal length and numerical aperture of the objective lens respectively, l_o is the index of the confocal z-slice containing an image of the basilar apodeme (the structure that we brought into focus during imaging) and w is a constant that was added to account for motion blur and manually set to 6μm to match the amount of blur we observed at the focal plane. For each fly,

the spatial models in the columns of **X** were registered with the calcium imaging stream, **Y**, using a single affine transformation for all frames. As registration markers, we selected the base of three large machrochaetes easily identified on both the confocal stack as well our calcium image sequence. We first background subtracted the images in **Y** by subtracting the average image of 100 frames before flight onset and solved for the coefficients in **B** using the scipy implementation of a non-negative least squares optimization algorithm.

The amount of spatial overlap between the elements of the anatomical model (columns of **X**) was evaluated using the pair-wise cosine distance (1/cosine similarity) between each column. The matrix of pair-wise distances was then clustered using the scipy (www.scipy.org) implementation of the WPGMA hierarchical method.